Available online at www.sciencedirect.com
SCIENCE DIRECT®
Journal of Solid State Chemistry 177 (2004) 2617–2627
JOURNAL OF SOLID STATE CHEMISTRY
http://elsevier.com/locate/jssc

$La_6Mo_8O_{33}$: a new ordered defect scheelite superstructure

V. Brizé,[a] S. Georges,[a] S. Kodjikian,[a] E. Suard,[b] and F. Goutenoire[a,*]

[a] *Faculté des Science, Laboratoire des Fluorures, UMR-CNRS 6010, Université du Maine, Avenue Olivier Messiaen, 72085 Le Mans Cedex 9, France*
[b] *Institut Laue Langevin, Avenue des Martyrs, B.P 156, 38042 Grenoble Cedex 9, France*

Received 23 September 2003; received in revised form 8 January 2004; accepted 4 March 2004

Abstract

The structure of $La_6Mo_8O_{33}$ has been determined from a triple pattern powder diffraction analysis. Two high-resolution neutron diffraction patterns collected at 1.594 and 2.398 Å and one X-rays were used. This molybdate crystallizes in a non-centrosymmetric monoclinic space group $P2_1(N°4)$, $Z = 2, a = 10.7411(3)$ Å, $b = 11.9678(3)$ Å, $c = 11.7722(3)$ Å, $\beta = 116.062\ (1)°$. $La_6Mo_8O_{33}$ is an unusual ordered defect Scheelite. Hence, it should be described with cation vacancies and an extra oxygen atom following the formula: $La_6\square_2Mo_8O_{32+1}$. This extra oxygen atom leads to a pyramidal environment, whereas the other molybdenum atoms present tetrahedral environment. A molybdenum tetrahedral is connecting to the pyramid, forming an $[Mo_2O_9]$ unit.

Keywords: Ordered defect Scheelite; Structural determination; High-resolution electron microscopy; X-ray and neutron diffraction

1. Introduction

The Scheelite structure is known as $CaWO_4$; it crystallizes in a tetragonal symmetry $I4_1/a$ ($a = 5.456(2)$ Å, $c = 12.020(2)$ Å). This structural type is adopted by a large family of compounds with different oxidation states for the both cations [1]. The Scheelite mineral is obtained with a couple of cations for which oxidation states are (II, VI), but several configurations are possible: (I–VII, III–V and IV–IV) respectively for $AgIO_4$, $YNbO_4$ and $ZrGeO_4$.

Only a few ordered defect Scheelite-type structures have been reported. In this case the structure is cation deficient with a formula $A_{2/3}\square_{1/3}MO_4$ [2–6] (A(III) = trivalent rare earth and M(VI) = Mo or W). All the structures are summarized in Table 1).

Recently an ordered defect Scheelite with the formula $A_{1.875}\square_{0.125}MO_4$ has been investigated in the Pb–W–O system. The compound could be described as $Pb_{7.5}\square_{0.5}W_8O_{32}$ [7]. It seems that the lead vacancy is due to the oxidation of 1/16 of lead atoms.

The main physical property associated with the Scheelite structural type is the luminescence of $PbWO_4$, and its potential use as a scintillator in detectors. Recently, the same compound ($PbWO_4$), substituted by lanthanum, has been evidenced as a good oxide ion conductor. The ionic conduction property is supposed to be the consequence of the interstitial extra oxygen formulated as $x/2$ in $Pb_{1-x}La_xWO_{4+x/2}$, the latter coming from the substitution of Pb^{2+} by a cation with a higher oxidation state La^{3+} [8–10].

Our group has investigated the MoO_3–La_2O_3 phase diagram for a few years. Two compounds have been synthesized and characterized: $La_2Mo_4O_{15}$ [11] and $La_2Mo_2O_9$ [12,13]. The latter presents the same structure as $SnWO_4$, and is a fast oxide-ion conductor [14].

Here, we present the synthesis, and the physical and structural characterization of a new phase with the formula $La_6Mo_8O_{33}$.

2. Experimental

X-ray diffraction patterns were collected on a Bragg-Brentano diffractometer (D8 Bruker-AXS). For the final compound, a longer diffraction pattern was collected, with an increment step of 0.02° (2θ) and a collecting time of 20 s per step, leading to a total data collecting time of 12 h. The neutron diffraction patterns of $La_6Mo_8O_{33}$ were collected on the Debye-Sherrer diffractometer D2B (instrument at ILL, Grenoble). Two

*Corresponding author. Fax: +33-243-8336-05.
E-mail address: francois.goutenoire@univ-lemans.fr (F. Goutenoire).

0022-4596/$ - see front matter © 2004 Elsevier Inc. All rights reserved.
doi:10.1016/j.jssc.2004.03.016

Table 1
Crystallographic parameters of different Scheelite-related structures

Name	a (Å)	b (Å)	c (Å)	β (deg)	Space group	Volume (Å^3)	Lattice parameters
$CaWO_4$	5.243	5.243	11.376	90.0	$I4_1/a$	313	$a_s \times b_s \times c_s$
$La_2Mo_3O_{12}$ [2]	17.006	11.952	16.093	108.4	$C2/c$	3103	$a_s\sqrt{10} \times c_s \times 3a_s$
$Ce_2W_3O_{12}$ [3]	7.813	11.72	11.58	109.4	$C2/c$	1000	$a_s\sqrt{2} \times c_s \times a_s\sqrt{5}$
$La_2W_3O_{12}$ [4]	7.813	11.841	11.654	109.3	$C2/c$	1026	$a_s\sqrt{2} \times c_s \times a_s\sqrt{5}$
$Eu_2W_3O_{12}$ [5]	7.676	11.463	11.396	109.6	$C2/c$	944.5	$a_s\sqrt{2} \times c_s \times a_s\sqrt{5}$
$Bi_2Mo_3O_{12}$ [6]	7.710	11.531	11.972	115.3	$P2_1/c$	962	$a_s\sqrt{2} \times c_s \times a_s\sqrt{5}$
$Pb_{7.5}W_8O_{32}$ [7]	7.716	7.716	12.020	90.0	$P4/nnc$	716	$a_s\sqrt{2} \times a_s\sqrt{2} \times c_s$

data collections were performed at 1.594 and 2.398 Å on $\sim$15 g of compound. For both the patterns the increment step was 0.05° (2θ), the interval of data collection ranging from 0° to 162°, the total counting time was $\sim$2 and $\sim$10 h, respectively, for 1.594 and 2.398 Å. For 2.398 Å a graphite filter was used.

The electron diffraction study was performed on a 200 kV side entry JEOL2010 transmission electron microscope with a double-tilt specimen holder operating at room temperature. For specimen preparation, a small amount of powder was ground in an agate mortar and pestle under dry methanol to produce a suspension. A drop of the suspension was deposited on a holey carbon film supported by a 1000 mesh copper grid and dried.

The thermal analysis of the compounds was performed on a differential thermal analysis (DTA) coupled with a thermo gravimetric analysis (TGA) apparatus (STD 2960, TA Instrument). The heating and the cooling rates of 15°C/min were applied on approximately 40 mg of compound. Normalization was realized in order to compare the area of the endothermic peaks.

The density measurements were performed on a gas picnometer ACCUPIC 1330 (Micromeritics) with helium as gas. The temperature of measurement was 22°C$\pm$1°C; for each measurement an amount between 1 and 1.5 g of the compound was used.

The transport property was studied by impedance spectroscopy using a Schlumberger Solartron SI 1260 frequency response analyzer with 0.1 V amplitude signal over the 32 MHz–0.1 Hz frequency range. A 5 mm diameter pellet was used for measurements with, as electrodes, platinum deposited on both faces.

3. Results and discussion

3.1. Synthesis

Different compounds with the composition $La_2Mo_{2+x}O_{9+3x}$, from $x=0$ ($La_2Mo_2O_9$) to $x=1$ ($La_2Mo_3O_{12}$) were prepared with La_2O_3 and MoO_3 as starting oxides. Lanthanum oxide powder was dried and decarbonated at 1000°C overnight prior to use. $La_2Mo_{2+x}O_{9+3x}$ compounds were synthesized from stoichiometric composition of both oxides. The weighted powders were grounded in an agate mortar for a few minutes and then finally placed in an alumina crucible. The powders were heated for several days at 800°C; no particular condition was used in order to cool down the samples. From the X-ray powder diffraction patterns (Fig. 1), we can observe around a nominal composition between ($0.2 \leqslant x \leqslant 0.6$) the appearance of new peaks which could not be indexed in $La_2Mo_2O_9$ or in $La_2Mo_3O_{12}$ patterns. These peaks could be observed at a low angle, especially two doublets around 12° and 17.5°. As $La_2Mo_3O_{12}$ is a large defect Scheelite structure which gives a great number of peaks, even at a low angle, the appearance of the new compound could be nicely observed only around these two angles (12° and 17.5°).

At this point, we have studied the best synthesis conditions for the new phase. From a nominal composition of $x=0.4$ ($La_2Mo_{2.4}O_{10.2}$) different attempts were made at 700°C, 800°C, 850°C and 900°C. The X-ray diffraction study shows that for the compounds synthesized at 700°C and 900°C the new phase is not present. For the compound synthesized at 850°C, the X-ray data present the peaks of the new phase and those of $La_2Mo_3O_{12}$. The optimal synthesis temperature seems to be 800°C$\pm$25°C. This synthesis temperature is relatively low compared to that of $La_2Mo_2O_9$ ($\sim$950°C) and $La_2Mo_3O_{12}$ ($\sim$1050°C), as observed in the phase diagram reported by Fournier et al. [15].

The synthesis temperature of $La_6Mo_8O_{33}$ is comparable with the low temperature of synthesis of $La_2Mo_4O_{15}$ (570–600°C). For the latter a thermal degradation is observed above $\sim$650°C.

3.2. Electron diffraction

The reciprocal lattice reconstruction, performed by electron diffraction allowed us to determine the new phase cell parameters:

$a \approx 10.7$ Å, $b \approx 12.0$ Å, $c \approx 11.7$ Å and $\beta \approx 116°$.

The electron diffraction patterns of the three basal planes could be indexed with the previous parameters

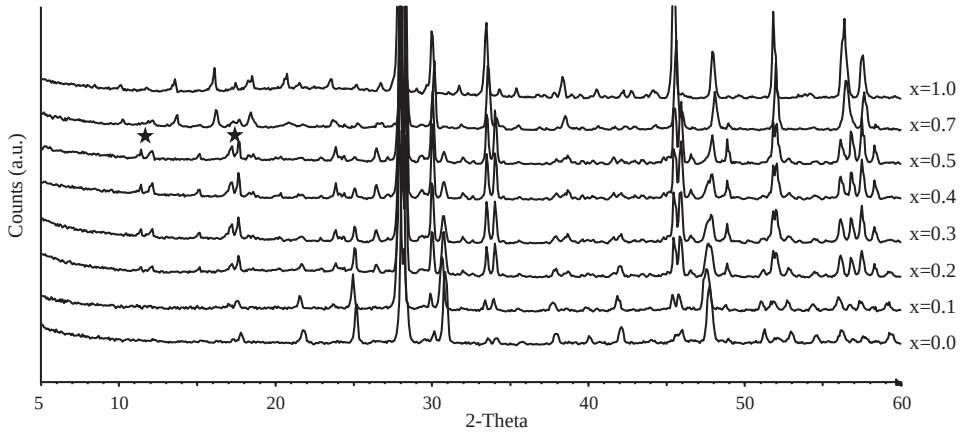

Fig. 1. Part of X-ray diffraction patterns of $La_2Mo_{2+x}O_{9+3x}$ for ($x = 0.0$, 0.1, 0.2, 0.3, 0.4 0.5, 0.7 and 1.0). The diffraction patterns of $La_2Mo_2O_9$ and $La_2Mo_3O_{12}$ are, respectively, obtained for $x = 0.0$ and $x = 1.0$. The asterisks present the two doublets of the $La_6Mo_8O_{33}$ compound.

(Fig. 2). The observed reflection condition during the reciprocal lattice reconstructions was $0\,k\,0$: $k = 2n$, leading to the two monoclinic space groups: $P2_1/m$ (No. 11) and $P2_1$ (No. 4). Note that the weak $0\,k\,0$ reflections with $k = 2n + 1$ are observed in the $[001]^*$ and $[100]^*$ electron diffraction patterns due to double diffraction. On all the observed diffraction patterns, we can notice a group of strong spots and a group of weak spots (Fig. 2a and b). These strong spots correspond to the Scheelite sub-cell. On the $[010]^*$ electron diffraction pattern (Fig. 2c and d), the strong spots could be indexed on a Scheelite cell, with $a_{\text{Scheelite}} \sim 5.4$ Å and $b_{\text{Scheelite}} \sim 5.4$ Å. The Scheelite crystallizes in the $I4_1/a$ space group (No. 88), with the reflection conditions: $h\,k\,l, h + k + l = 2n; h\,k\,0, h, k = 2n$ and $00\,l$, $l = 4n$. Then, the strong spots correspond to the $h\,k\,0$ peaks with the $h, k = 2n$ as reflection condition (Fig. 2d).

From the cell parameters analysis and from this Scheelite sub-cell evidence, the relation between the cell parameters of the new phase (np) and the Scheelite (S) structure was proposed as

$$|\vec{a}_{\text{np}}| = |2\vec{a}_{\text{S}}|, \left|\vec{b}_{\text{np}}\right| = |\vec{c}_{\text{S}}| \text{ and } |\vec{c}_{\text{np}}| = \left|2\vec{b}_{\text{S}} - \vec{a}_{\text{S}}\right|.$$

In the reciprocal space, the cell parameters are deduced from the normal matrix calculation.

$$\left|\vec{a}^*_{\text{np}}\right| = \left|\tfrac{1}{2}\vec{a}^*_{\text{S}} + \tfrac{1}{4}\vec{b}^*_{\text{S}}\right| \left|\vec{b}^*_{\text{np}}\right| = \left|\vec{c}^*_{\text{S}}\right| \text{ and } \left|\vec{c}^*_{\text{np}}\right| = \left|\tfrac{1}{2}\vec{b}^*_{\text{S}}\right|.$$

3.3. Analysis of the La/Mo ratio deduced from the DTA measurement

As seen in the synthesis paragraph, the new phase was observed by X-ray diffraction around the nominal composition ($0.2 \leqslant x \leqslant 0.6$) for $La_2Mo_{2+x}O_{9+3x}$. From the electron diffraction paragraph, the cell parameters relations between the new phase and the Scheelite led to a volume of the new cell four times bigger than the Scheelite one. As the unit formula per cell (Z) is four in the Scheelite structure, $A_{16}B_{16}X_{64}$ is then the formula of the new phase, with some vacancies on the A site. The link between theses two analyses was not so evident. Here, the DTA measurements help us to determine a better La/Mo ratio for the new phase.

The DTA measurements were performed for all the compositions from $x = 0.0$ to $x = 0.7$ and $x = 1.0$. For all, endothermic and exothermic peaks were observed, respectively, during the heating and the cooling, except $x = 0.7$ and $x = 1.0$ (Table 2). The $La_2Mo_2O_9$ ($x = 0.0$) compound presents a phase transition around 580°C from an α monoclinic to a β cubic structure [14]. The $La_2Mo_3O_{12}$ compound ($x = 1.0$) does not present any phase transition or thermal evolution. In order to obtain a linear behavior of the Tammann curve, we transformed x in the molar fraction of MoO_3, $\%MoO_3 = (2 + x)/(3 + x) \times 100$ in the phase diagram La_2O_3–MoO_3. The plot (Fig. 3) represents the Tammann curve of the phase transition of $La_2Mo_2O_9$. When the fraction of $La_2Mo_2O_9$ is equal to zero, the area of the phase transition is also equal to zero; consequently it is also the composition of the new phase. The solution of the linear regression is found for 72.64% leading to $x = 0.655$. It gives the cationic composition $La_2Mo_{2.655}$. In order to match this value to the formula $A_{16}B_{16}X_{64}$, we have to multiply x by 6.026, nearly a perfect integer ~ 6. To complete this analysis, different compounds with the following compositions: $La_2Mo_{2.60}O_{10.80}$, $La_2Mo_{2.63}O_{10.89}$, $La_2Mo_{2.66}O_{10.98}$ and $La_2Mo_{2.70}O_{11.1}$ were synthesized and analyzed by X-ray diffraction (Fig. 4). The compound with the formula $La_2Mo_{2.66}O_{10.89}$ was found to have the best purity, confirming the cationic formula deduced from DTA measurements.

3.4. Symmetry

From the electron diffraction analysis, two space groups were found to be appropriate to match with the

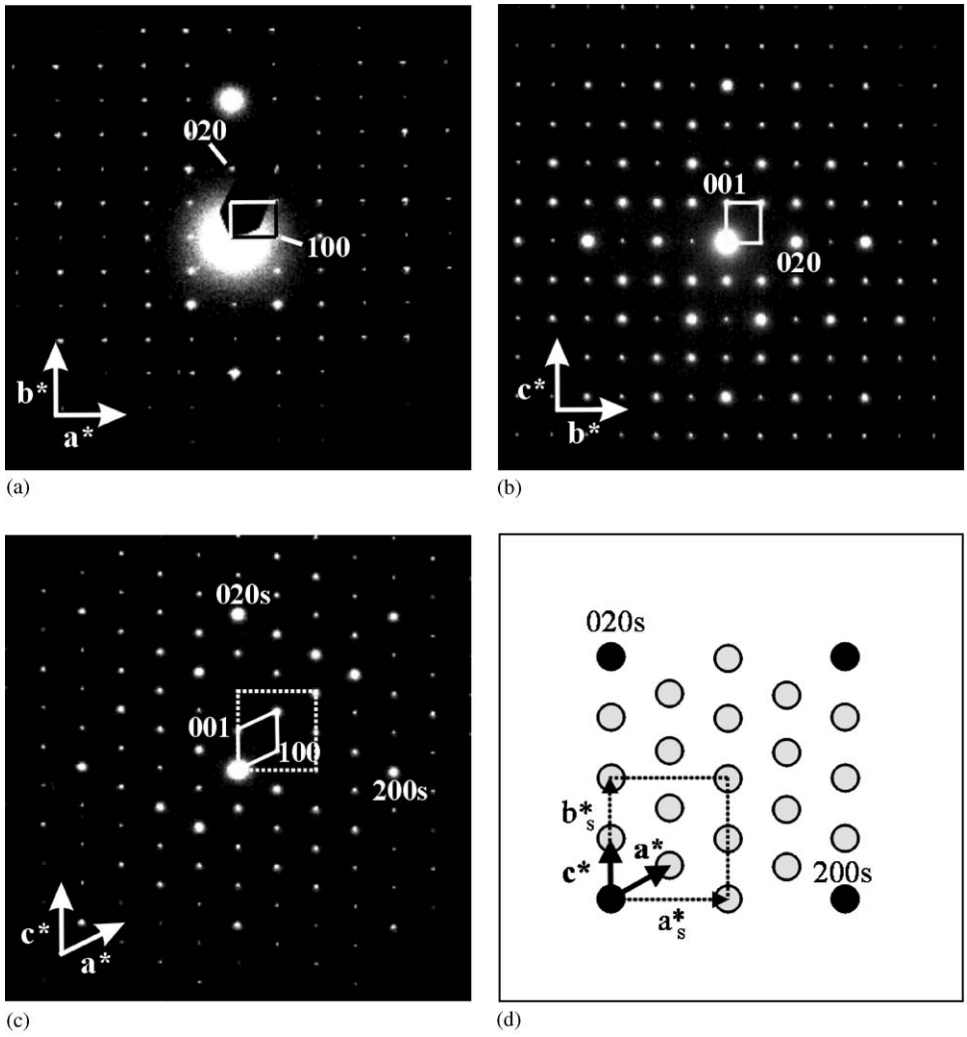

Fig. 2. Electron diffraction patterns of $La_6Mo_8O_{33}$ along (a) $[001]^*$, (b) $[100]^*$, (c) $[010]^*$. (d) Schematic drawing of the electron diffraction pattern of $La_6Mo_8O_{33}$ compound along $[010]^*$; the large spots represent the Scheelite sub-cell along $[001]^*$ Scheelite.

monoclinic parameters and the extinction rules: $P2_1$ (No. 4) non-centrosymmetric and $P2_1/m$ (No. 11) centrosymmetric. In order to choose between these two space groups, a diagram of the cationic positions of the Scheelite sub-cell was made (Fig. 5). It appears that the 2_1 axis can be placed at $x = 1/4$, $y = 1/4$ parallel to the c-axis. In the centrosymmetric space group $P2_1/m$, the center of symmetry -1 is placed on the 2_1 axis. From the simple analysis of the cation positions in the Scheelite structure, it appears that no solution was found in order to match an acceptable position $(1/4, 1/4, z)$ for a center of symmetry. Another clue came from the analysis of the space groups of the different ordered defect Scheelite structures and the Scheelite itself. These crystallize in four different space groups: $I4_1/a$ (No. 88), $C2/c$ (No. 15), $P2_1/c$ (No. 14) and $P4/nnc$ (No. 126) (Table 1). In the first space group the -1 symmetry center is not placed on the 4_1 axis but on a 4 axis. The same analysis can be done on the $C2/c$ and $P2_1/c$ space groups, where the 2_1 axis and the -1 are not placed together. For the last space group $P4/nnc$, in the second setting which is centrosymmetric, the 4 or the -4 axis is not placed with the -1 center.

3.5. Structural characterization

In the first step, the cationic structure of the new phase was deduced from the Scheelite subcell. The (x, y, z) positions of the cations were calculated from the transformation matrix following the equation:

$$\begin{pmatrix} x \\ y \\ z \end{pmatrix} = Q \begin{pmatrix} x' \\ y' \\ z' \end{pmatrix} + \begin{pmatrix} -3/16 \\ 0 \\ -1/8 \end{pmatrix},$$

where the Q matrix is $Q = P^{-1}$. This leads to 8 lanthanum positions and 8 molybdenum positions. In order to determine the two lanthanum vacancies, to match with the cationic formula $La_6\square_2Mo_8$, all the $C_2^8 = 28$ models were tested. We have used the X-ray

Table 2
Results of DTA measurements obtained for $La_2Mo_{2+x}O_{9+x}$

x	Molar fraction % MoO_3	Area a.u. (°C min^{-1})	Transition (°C)	Weighted powder (mg)	Corrected area a.u. (°C min^{-1})
0.0	66.67	0.322	583.8	44.78	0.288
0.2	68.75	0.176	581.6	38.37	0.184
0.3	69.70	0.133	579.4	38.07	0.140
0.4	70.59	0.099	580.1	41.03	0.096
0.5	71.43	0.061	577.8	41.85	0.059
0.6	72.22	0.019	578.0	36.16	0.021

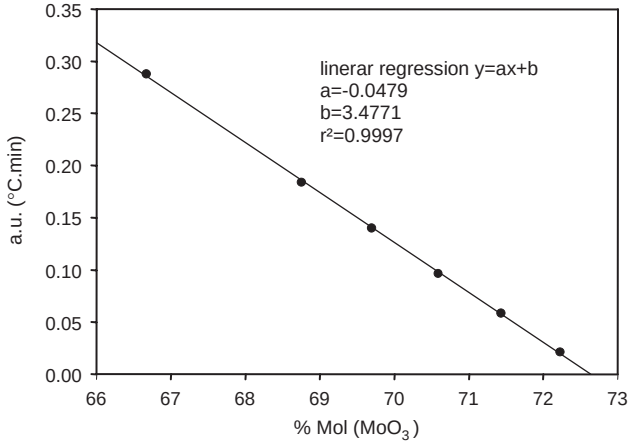

Fig. 3. Evolution of the peak area of the endothermic signal (DTA) versus the molar fraction of MoO_3; the points represent the measurements, and the black line represents the linear regression.

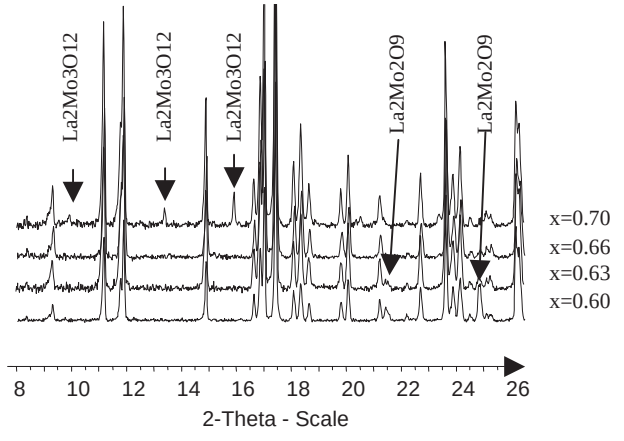

Fig. 4. X-ray diffraction patterns of $La_2Mo_{2+x}O_{9+3x}$ for $x = 0.60$, 0.63, 0.66 and 0.70. The impurities are marked with arrows. The compound with the composition $La_2Mo_{2.66}O_{10.89}$ does not present $La_2Mo_2O_9$ nor $La_2Mo_3O_{12}$ impurities.

diffraction pattern from 8° to 60°, the only parameters refined are the cell parameters and profile parameters, not the cationic position. The refinement of the model without vacancies lead to $R_{\text{Bragg}} = 21.6\%$ and $R_{\text{wp}} = 52.6\%$. The different models with two vacancies on the Lax and Lay positions gave a series of $R_{\text{Bragg}}(x, y)$ and $R_{\text{wp}}(x, y)$. The maximum was found

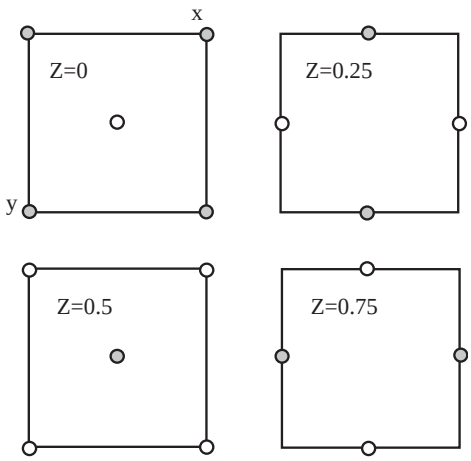

Fig. 5. Schematic drawings of the cations in the Scheelite structure along the c-axis. The different sections ($z = 0.0$, 0.25, 0.50 and 0.75) are drawn. The black and white circles represent the calcium and the tungsten atoms, respectively.

for (6,7) vacancies positions, with $R_{\text{Bragg}}(6,7) = 38.4\%$ and $R_{\text{wp}}(6,7) = 53.4\%$ and the two lowest minimums for $R_{\text{Bragg}}(2,5) = R_{\text{Bragg}}(4,7) = 28.5\%$ and $R_{\text{wp}}(2,5) = 39.5\%$. These two minima were significantly lower than all other $R_{\text{Bragg}}(x, y)$ and R_{wp} factors. The second lowest factor was found for (1,8) with $R_{\text{Bragg}} = 31.3\%$ and $R_{\text{wp}} = 49.2\%$, confirming the real minimum of the previous two solutions. It appears by a simple drawing of the lanthanum vacancies (Fig. 6), that these two solutions are slightly equivalent. In fact, in both the solutions the projections along the b-axis of the lanthanum vacancies are forming pseudolines parallel to the large diagonal of the monoclinic cell. We chose the (4,7) solution arbitrarily. In the second step, the 32 oxygen atoms positions deduced from the Scheelite subcell were added. In order to refine this large structure; 8 molybdenum atoms, 6 lanthanum atoms and 32 oxygen atoms leading to 137 adjustable atomic parameters, we have used for the refinement the three powder diffraction patterns, one X-ray and two neutron. The simultaneous refinement was carried out using the program Fullprof [16]; the weighting scheme used was 33.3%, 33.3% and 33.3%. During the refinement, the global relaxation factor for the atomic

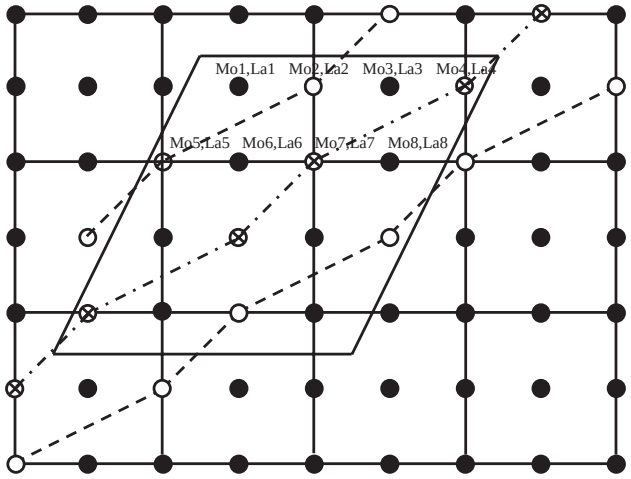

Fig. 6. Schematic drawings of the Scheelite structure along the *c*-axis. For clarity, only cations have been drawn (Ca and W atoms in black). The small squares present the cell of the Scheelite sub-cell. The cell of the $La_6Mo_8O_{33}$ is drawn. The different cationic positions of the lanthanum and molybdenum are labeled. The lanthanum vacancies (2,5) and (4,7) are presented with white circles; dotted lines are drawn to guide the eyes.

Table 3
Characteristics of the refinement conditions

Diffractometer	D2B(ILL)	D2B(ILL)	Bruker D8-AXS
Radiation	Neutron	Neutron	X-ray
Wavelength (Å)	1.59481(5)	2.39815(7)	K_α(Cu)
2θ range (deg)	7–160	7–160	7–94
R_{Bragg} (%)	4.29	4.00	8.60
R_p (%)	7.35	5.95	14.2
R_{wp} (%)	9.15	7.32	16.2
R_{exp} (%)	3.33	2.78	6.93
χ^2	7.55	6.95	5.49
Number of reflections	2820	845	1298

shifts was reduced to 10%; this allowed the refinement of the 137 atomic parameters without problems. After subsequent refinement cycles, an atomic residue appeared in the Fourier difference map. This Fourier difference map was calculated with the program Gfou [17], using the neutron diffraction data ($\lambda = 2.398$ Å). This extra oxygen completes the molybdenum Mo4 coordination and it satisfies the formula: $La_6Mo_8O_{33}$. At the final stage, all the atomic positions and the profile parameters were refined. Due to the strong overlap of the measured peaks and the large number of the atomic refined positions, we fixed the atomic displacement parameters by type of atoms, i.e., molybdenum, lanthanum and oxygen. These last refinements lowered the different reliability factors, all refinement parameters are summarized in Table 3. The final atomic positions are given in Table 4, and the result of the diffraction refinement is presented in Fig. 7a–c.

Table 4
Crystallographic parameters of $La_6Mo_8O_{33}$

Atom	*x*	*y*	*z*
Mo1	0.187(2)	0.490(2)	0.130(2)
Mo2	0.433(2)	0.232(2)	0.122(2)
Mo3	0.677(2)	0.494(2)	0.122(2)
Mo4	0.937(2)	0.217(2)	0.122(2)
Mo5	0.069(2)	0.000(2)	0.397(2)
Mo6	0.303(2)	0.759(2)	0.367(2)
Mo7	0.561(2)	−0.003(2)	0.363(2)
Mo8	0.824(2)	0.750(2)	0.376(2)
La1	0.162(1)	0.000	0.118(1)
La2	0.426(1)	0.750(1)	0.123(1)
La3	0.715(1)	−0.010(1)	0.107(1)
La5	0.055(1)	0.504(1)	0.345(1)
La6	0.326(1)	0.246(1)	0.390(1)
La8	0.802(1)	0.243(1)	0.362(1)
O1	0.201(2)	0.391(2)	0.025(2)
O2	0.333(2)	0.592(2)	0.165(2)
O3	0.231(2)	0.425(2)	0.284(2)
O4	0.008(2)	0.518(2)	0.104(2)
O5	0.440(2)	0.320(2)	−0.003(2)
O6	0.581(2)	0.152(2)	0.196(2)
O7	0.430(2)	0.302(2)	0.254(2)
O8	0.293(2)	0.146(2)	0.051(2)
O9	0.316(2)	0.923(2)	0.009(2)
O10	0.822(2)	0.571(2)	0.212(2)
O11	0.660(2)	0.383(2)	0.215(2)
O12	0.508(2)	0.570(2)	0.053(2)
O13	0.077(2)	0.793(2)	0.003(2)
O14	0.126(2)	0.177(2)	0.207(2)
O15	0.951(2)	0.308(2)	0.257(2)
O16	0.752(2)	0.191(2)	0.091(2)
O17	0.103(2)	0.920(2)	0.293(2)
O18	0.205(2)	0.102(2)	0.461(2)
O19	0.065(2)	0.925(2)	0.526(2)
O20	0.911(2)	0.080(2)	0.306(2)
O21	0.321(2)	0.840(2)	0.247(2)
O22	0.449(2)	0.680(2)	0.421(2)
O23	0.290(2)	0.819(2)	0.499(2)
O24	0.180(2)	0.665(2)	0.309(2)
O25	0.571(2)	0.922(2)	0.235(2)
O26	0.276(2)	0.571(2)	0.555(2)
O27	0.448(2)	0.403(2)	0.531(2)
O28	0.396(2)	0.077(2)	0.299(2)
O29	0.852(2)	0.846(2)	0.276(2)
O30	0.020(2)	0.166(2)	0.550(2)
O31	0.189(2)	0.331(2)	0.497(2)
O32	0.662(2)	0.690(2)	0.293(2)
O33	0.916(2)	0.059(2)	0.066(2)

Note: Space group $P2_1$ (No. 4), $Z = 2$.
Cell parameters: $a = 10.7411(3)$ Å, $b = 11.9678(3)$ Å, $c = 11.7722(3)$ Å, $\beta = 116.062(1)°$.
All atomic sites (2*a*) are fully occupied, atomic displacement factors were constrained by type of atoms: B (Mo) = 0.65(5) Å^2, B (La) = 0.30(4) Å^2, B (O) = 0.60(2) Å^2.

At this final stage, the presence of the extra oxygen O_{33} was verified. Only the neutron diffraction pattern collected at $\lambda = 2.398$ Å was used, and no atomic and profile parameters were refined. The reliability factor obtained for the model without O_{33} was subsequently

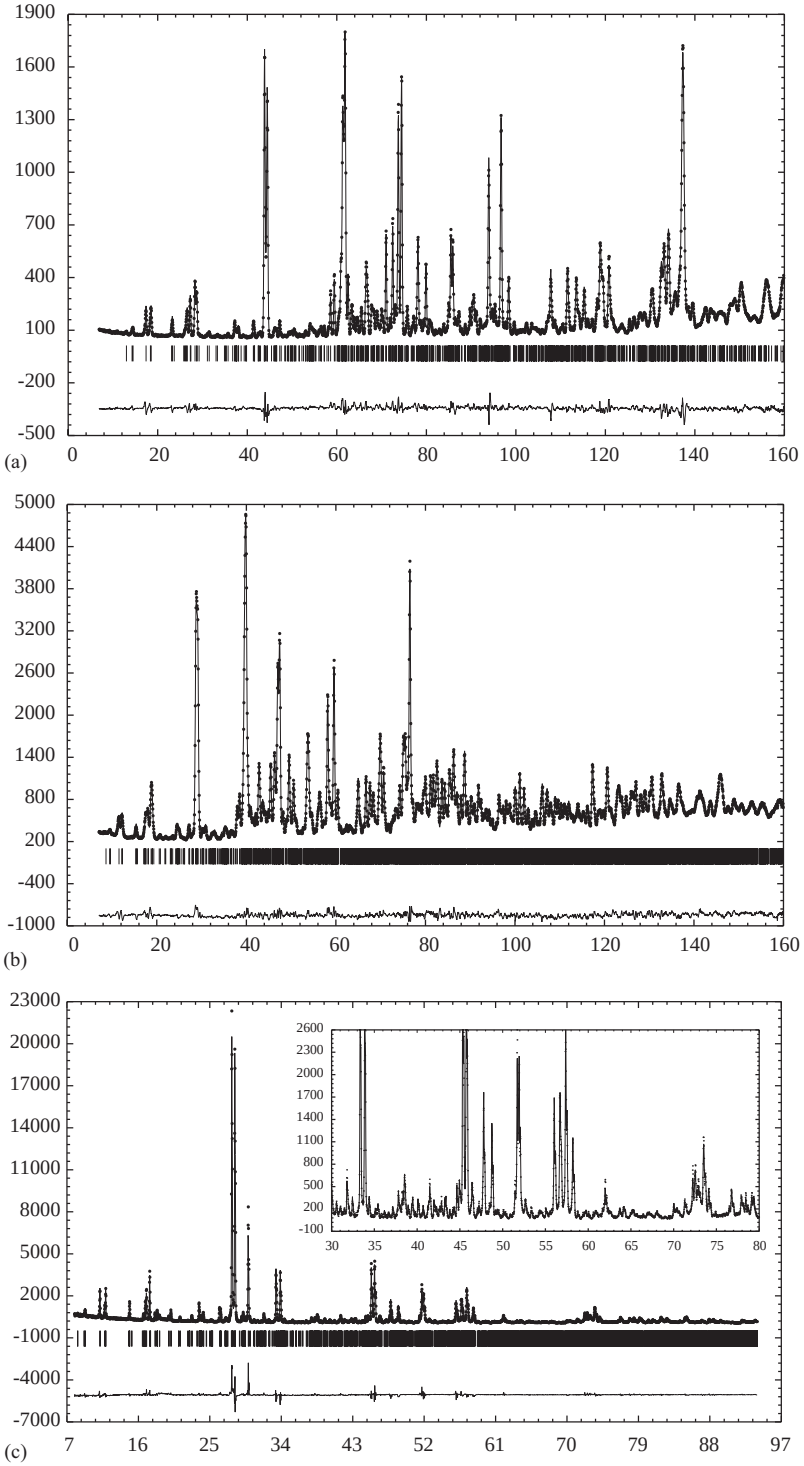

Fig. 7. Result of the final refinement of $La_6Mo_8O_{33}$: observed (dot), calculated (line) and difference at bottom. Neutron diffraction patterns collected at (a) 2.398 Å. (b) 1.594 Å. (c) X-ray diffraction pattern. Inset: close-up of the intermediate 2θ.

larger, $R_{Bragg} = 7.69\%$, than the one obtained with O_{33}, $R_{Bragg} = 4.29\%$.

Another information came with the density measurement. The average of three different measurements gave 5.164 (1) g/cm^3. The problem of the exact formula of this new compound could be solved by this analysis of different parameters and hypotheses. The single hypothesis is the oxidation number of the molybdenum which has been fixed to $+6$. It seems spurious to expect a smaller oxidation number for this molybdenum oxide

Table 5
Results of the different calculated densities

Cases	Formula	Molecular weight	Calculated density	$2n_{Mo}/n_{La}$
1	$La_6Mo_8O_{33}$	2128.9	5.20	2.66
2	*$La_6Mo_8O_{32}$*	*2112.9*	*5.16*	*2.66*
3	$La_{5.333}Mo_8O_{32}$	2020.3	4.94	3.00
4	$La_6Mo_{7.66}O_{32}$	2080.3	5.08	2.55
5	$La_{5.818}Mo_{7.758}O_{32}$	2064.4	5.04	2.66

Cell volume: 1359.4 Å^3. Hypotheses are given by the formula. The italic characters indicate that the molybdenum oxidation state is lower than +6.

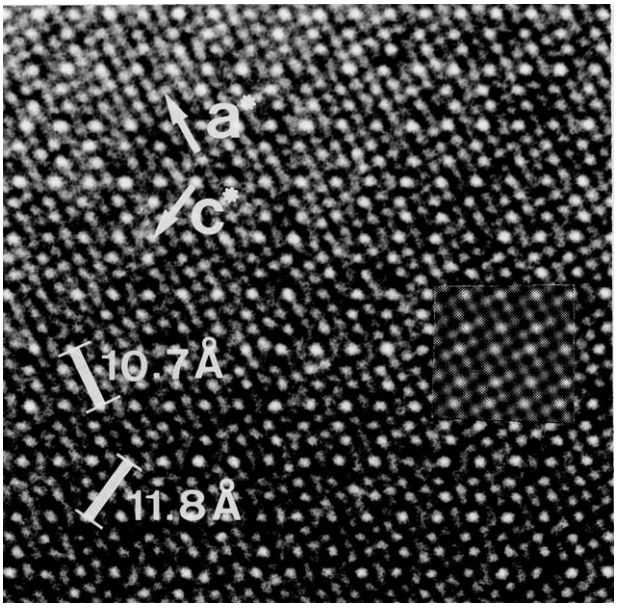

Fig. 8. HREM image of $La_6Mo_8O_{33}$ along the [0−10] zone. A calculated image for a defocus of 300 Å and a thickness of 24 Å is shown as an inset.

prepared in air. The different parameters are the molybdenum lanthanum ratio and the total oxygen content. Different cases are proposed in Table 5. It appears that all the cases from 2 to 5, where we have forced the oxygen content to be equal to 32 are, for case 2, spurious due to the absence of molybdenum +6, and for cases 3–5 the calculated density is slightly lower than the measured one. Usually, the calculated density is slightly larger than the measured one.

3.6. High-resolution electron microscopy

The new phase $La_6Mo_8O_{33}$ is unstable and decomposes under an intense electron beam. This does not affect the recording of the diffraction patterns, but severely disturbs the acquisition of HREM images. To limit this problem, an electron beam was spread and a relatively long exposure time was used (2 s), leading to quite noisy images.

The [0−10] HREM image presented in Fig. 8 shows regular contrasts on a large zone. It suggests that the compound is a quite well-ordered phase, without planar defects in (a, c) planes. The corresponding theoretical image was calculated on the basis of the positional parameters refined from XRD and neutron data (Table 4), using the E.M.S. program [18]. The simulated image

Table 6
Calculated bond valence

Atom	Calculated valence
Mo1	5.3(2)
Mo2	6.0(2)
Mo3	5.5(2)
Mo4	5.8(2)
Mo5	5.7(2)
Mo6	6.7(3)
Mo7	5.5(2)
Mo8	5.6(2)
La1	3.0(1)
La2	3.4(1)
La3	3.1(1)
La5	3.1(1)
La6	3.4(1)
La8	3.1(1)
O1	1.9(1)
O2	1.8(1)
O3	2.1(1)
O4	1.9(1)
O5	1.9(1)
O6	2.2(1)
O7	1.9(1)
O8	2.1(1)
O9	2.1(1)
O10	2.2(1)
O11	1.9(1)
O12	1.8(1)
O13	2.0(1)
O14	2.0(1)
O15	1.8(1)
O16	1.9(1)
O17	2.0(1)
O18	1.7(1)
O19	2.0(1)
O20	2.0(1)
O21	2.1(1)
O22	2.1(1)
O23	1.9(1)
O24	2.5(2)
O25	2.0(1)
O26	1.9(1)
O27	2.1(1)
O28	1.8(1)
O29	1.8(1)
O30	1.9(1)
O31	1.9(1)
O32	2.0(1)
O33	2.0(1)

Table 7
Selected bond distances (Å) for $La_6Mo_8O_{33}$

(Mo1)–(O1):1.77(3)	(La2)–(O2):2.29(3)
(Mo1)–(O2):1.89(3)	(La2)–(O5):2.59(3)
(Mo1)–(O3):1.83(3)	(La2)–(O9):2.46(3)
(Mo1)–(O4):1.85(3)	(La2)–(O12):2.60(3)
(Mo1)–(O33):2.24(3)	(La2)–(O16):2.50(3)
	(La2)–(O21):2.45(3)
(Mo2)–(O5):1.83(3)	(La2)–(O25):2.58(3)
(Mo2)–(O6):1.72(3)	(La2)–(O32):2.55(3)
(Mo2)–(O7):1.79(3)	
(Mo2)–(O8):1.70(3)	(La3)–(O1):2.43(3)
	(La3)–(O5):2.58(3)
(Mo3)–(O9):1.80(3)	(La3)–(O6):2.87(3)
(Mo3)–(O10):1.72(3)	(La3)–(O12):2.50(3)
(Mo3)–(O11):1.78(3)	(La3)–(O16):2.46(3)
(Mo3)–(O12):1.87(3)	(La3)–(O20):2.60(3)
	(La3)–(O25):2.71(3)
(Mo4)–(O13):1.69(3)	(La3)–(O29):2.55(3)
(Mo4)–(O14):1.89(3)	(La3)–(O33):2.55(3)
(Mo4)–(O15):1.88(3)	
(Mo4)–(O16):1.88(3)	(La5)–(O3):2.48(3)
(Mo4)–(O33):1.97(3)	(La5)–(O4):2.66(3)
	(La5)–(O10):2.44(3)
(Mo5)–(O17):1.70(3)	(La5)–(O15):2.59(3)
(Mo5)–(O18):1.80(3)	(La5)–(O19):2.56(3)
(Mo5)–(O19):1.79(3)	(La5)–(O24):2.51(3)
(Mo5)–(O20):1.82(3)	(La5)–(O26):2.70(3)
	(La5)–(O30):2.62(3)
(Mo6)–(O21):1.80(3)	(La5)–(O31):2.69(3)
(Mo6)–(O22):1.70(3)	
(Mo6)–(O23):1.77(3)	(La6)–(O3):2.46(3)
(Mo6)–(O24):1.63(3)	(La6)–(O7):2.41(3)
	(La6)–(O14):2.42(3)
(Mo7)–(O25):1.78(3)	(La6)–(O18):2.51(3)
(Mo7)–(O26):1.81(3)	(La6)–(O22):2.58(3)
(Mo7)–(O27):1.71(3)	(La6)–(O27):2.48(3)
(Mo7)–(O28):1.86(3)	(La6)–(O28):2.55(3)
	(La6)–(O31):2.54(3)
(Mo8)–(O29):1.77(3)	
(Mo8)–(O30):1.80(3)	(La8)–(O6):2.56(3)
(Mo8)–(O31):1.83(3)	(La8)–(O33):2.41(3)
(Mo8)–(O32):1.72(3)	(La8)–(O15):2.54(3)
	(La8)–(O19):2.62(3)
(La1)–(O4):2.46(3)	(La8)–(O20):2.51(3)
(La1)–(O8):2.58(3)	(La8)–(O23):2.44(3)
(La1)–(O9):2.66(3)	(La8)–(O26):2.57(3)
(La1)–(O13):2.77(3)	(La8)–(O30):2.60(3)
(La1)–(O14):2.46(3)	
(La1)–(O17):2.59(3)	
(La1)–(O21):2.57(3)	
(La1)–(O28):2.65(3)	
(La1)–(O33):2.53(3)	

for a defocus of 300 Å and a thickness of 24 Å is in good agreement with the observed image, confirming the structural model. Calculated images with and without O33 do not present any difference.

3.7. Structural analysis

This large structure presents 8 different molybdenum coordination polyhedra. Six of them could be considered as a regular tetrahedron environment, where the molybdenum oxygen distances range from 1.63 to 1.87 Å with an average distance of 1.77 Å (see Table 7). Only Mo1 and Mo4 present a slightly different environment due to the introduction of an extra oxygen in this structure. The Mo1-O33 distance is the biggest, with 2.24 Å; the other distances are also larger than the average distance reported before. As a consequence, the bond valence calculation for Mo1 is the lowest of the list reported in Table 6 with 5.3. The coordination polyhedra of Mo1 could be described as a distorted tetrahedron with an extra oxygen atom (Fig. 9). In comparison, the Mo4 coordination polyhedron is easier to describe; it is a pyramid with a square base.

The bond valence calculation was performed directly by the program Fullprof [16], using the Brown-Altermatt empirical expression: $\text{Valence} = \Sigma \exp(\text{Ro}-d)/B$ with $B = 0.37$ Å [19]. The values used by the Fullprof program were for La^{3+}–O^{2-} Ro = 2.172 Å and for Mo^{6+}–O^{2-} Ro = 1.907 Å [20].

For the molybdenum atoms the bond valence calculation gives values around the +6. There is a large difference between the smallest value obtained for Mo1 (5.3) and with the largest value obtained for Mo6 (6.7). Nevertheless the others values are much more regular and slightly lower than 6. This last observation has also been evidenced for $La_2Mo_4O_{15}$ [11]. Note the right bond valence calculation obtained for Mo4 with the extra oxygen (O33).

As in $La_2Mo_4O_{15}$, the bond valence calculation for the lanthanum atoms gives values slightly in excess of the expected +3 (see Table 6). The bond valence calculation obtained for the oxygen atoms range from 1.7 to 2.5 with an average of 1.98.

The projection of the structure along the *b*-axis in Fig. 10 is rather similar to the other ordered defect Scheelite [22], of the $Ln_2\square Mo_3O_{12}$ family. As these Scheelites, $La_6Mo_8O_{33}$ has to be described as $La_6\square_2Mo_8O_{33}$. But for our new compound the oxygen content has to be written as: $La_6\square_2Mo_8O_{32+1}$. The localization of this extra oxygen is not surprising. As there are two cationic vacancies, the extra oxygen O33 appears near the La4 vacancy. The starting atomic positions of La4 were: 0.9375; 0.7500; 0.1250; the atomic position refined for O33 are: 0.916, 0.059, and 0.066. The calculated distance between La4 vacancy and O33 was 3.75 Å. These results also confirmed the presence of the extra oxygen. Recently, Esaka et al. [8–10] have reported a Scheelite structure with extra oxygen following the formula: $Pb_{1-x}La_xW_2O_{4+x/2}$ with x ranging from 0 to 0.3. To our knowledge, this is the first time that a defect ordered Scheelite presents cation vacancies and extra oxygen at the same time.

Another interesting feature is the formation of a large unit of formula $[Mo_2O_9]$ shown in Fig. 11. This unit is formed by the Mo4 and Mo1 coordination polyhedra

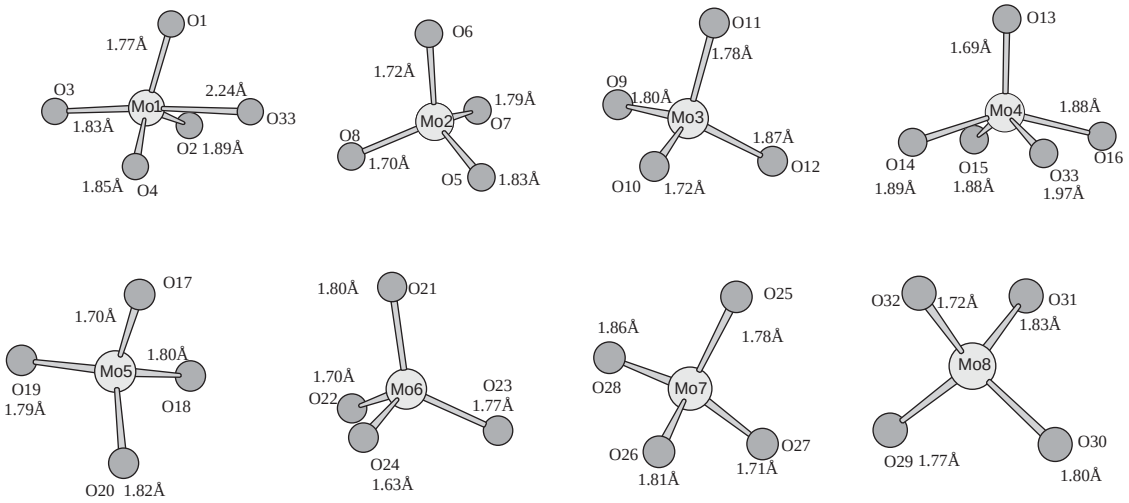

Fig. 9. Details of the 8 molybdenum coordination polyhedra. The molybdenum–oxygen distances are given without uncertainties.

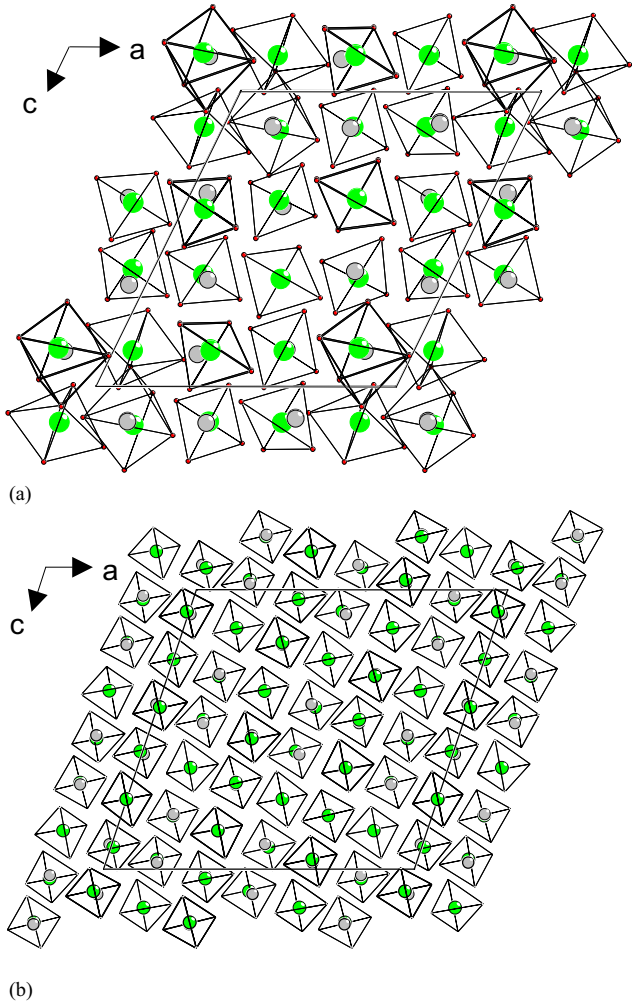

Fig. 10. Projection along the *b*-axis of (a) $La_6Mo_8O_{33}$ and (b) $La_2Mo_3O_{12}$.

which share the extra oxygen atom O33. These large units are common in molybdates. For example, $La_2Mo_4O_{15}$ is formed from $[Mo_6O_{22}]$ unit formed by

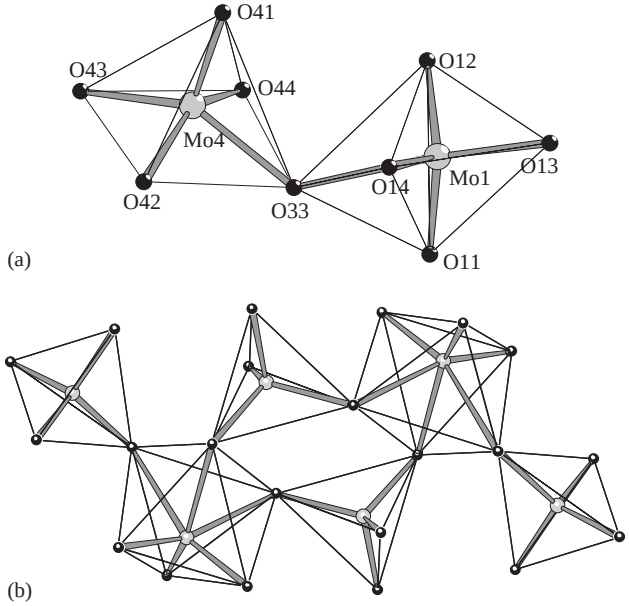

Fig. 11. Coordination polyhedra units observed (a) $[Mo_2O_9]$ unit in $La_6Mo_8O_{33}$ and (b) $[Mo_6O_{22}]$ unit in $La_2Mo_4O_{15}$.

two octahedra and four tetrahedra [11], with similar molybdenum–oxygen distances. Other examples are given in Wells [21] ($Na_2Mo_2O_7$ and $K_2Mo_3O_{10}$).

3.8. Impedance measurement

Fast oxide-ion conductors still attract attention due to their potential applications, especially in solid oxide fuel cell (SOFC). $La_2Mo_2O_9$ is a fast oxide-ion conductor, with an ionic conduction of $0.06\,S\,cm^{-1}$ at 800°C [14]. $La_6Mo_8O_{33}$ has been evidenced during this analysis of different compounds with the composition $La_2Mo_{2+x}O_{9+3x}$, from $x=0$ ($La_2Mo_2O_9$) to $x=1$ ($La_2Mo_3O_{12}$). This proximity with a great conductor encouraged us to study the ionic conduction of

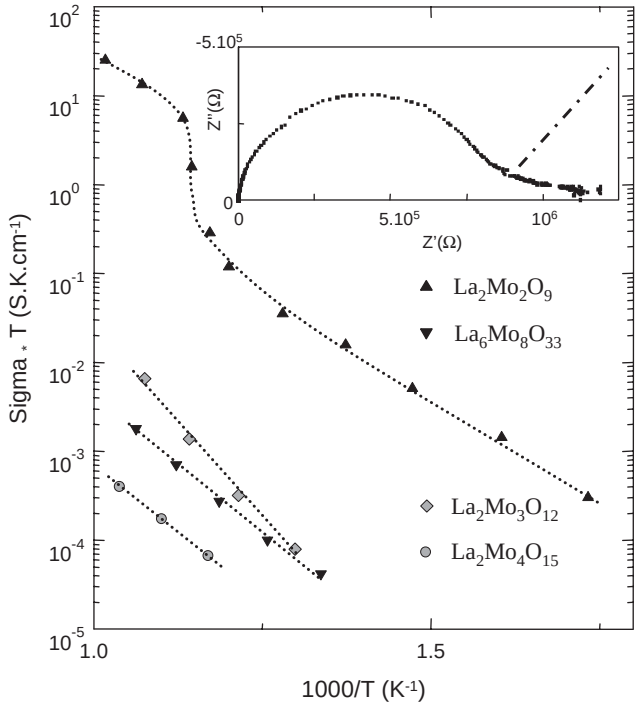

Fig. 12. Arrhenius plot of different compounds ($La_2Mo_2O_9$, $La_6Mo_8O_{33}$, $La_2Mo_3O_{12}$ and $La_2Mo_4O_{15}$); lines are drawn to guide the eyes. Inset: the Nyquist plot of $La_6Mo_8O_{33}$ at 668°C. The dashed line represents the Warburg behavior of the low-frequency impedance spectrum typically observed for ionic conductor.

$La_6Mo_8O_{33}$ by means of impedance spectroscopy. Fig. 12 shows the conductivity measurements of different lanthanum molybdates. The total conductivities of $La_6Mo_8O_{33}$, $La_2Mo_4O_{15}$ and $La_2Mo_3O_{12}$ are comparable but they are much lower than $La_2Mo_2O_9$, by at least two orders of magnitude, another feature not in favor of a possible oxide-ion conduction property of $La_6Mo_8O_{33}$. Usually, in oxide-ion conductors, the impedance at a low-frequency range presents a Warburg impedance [22]. Here, the Nyquist plot obtained at 668°C does not present such a feature (Fig. 12).

4. Conclusion

A new structure has been evidenced during the analysis of the system $La_2Mo_{2+x}O_{9+3x}$, from $x = 0$ ($La_2Mo_2O_9$) to $x = 1$ ($La_2Mo_3O_{12}$). This new compound appears in a narrow region around $x = 0.667$ leading to a formula of $La_6Mo_8O_{33}$. As $La_2Mo_3O_{12}$, which is an ordered defect Scheelite with cation vacancies, formulated as $La_2\square Mo_3O_{12}$ ($La_{2/3}\square_{1/3}MoO_4$). This compound could be described in a similar manner as $La_6\square_2Mo_8O_{33}$ ($La_{3/4}\square_{1/4}MoO_{4,125}$). But it is relatively different from other ordered defect Scheelites which only present cation vacancies. Here, $La_6Mo_8O_{33}$ has to be formulated as $La_6\square_2Mo_8O_{32+1}$. To our knowledge, this is the first time that there are cation vacancies and extra oxygen atoms at the same time. This extra oxygen atom leads to a pyramidal environment of Mo4 and creates a large unit of formula [Mo_2O_9]. The physical properties have been explored; $La_6Mo_8O_{33}$ does not exhibit any oxide-ion conduction property.

References

[1] R.W.G. Wyckoff, Crystal Structures, 2nd Edition, Interscience Publishers, New York, p. 19 (Chap. VIIIA).
[2] W. Jeitschko, Acta Crystallogr. B 29 (1973) 2074–2081.
[3] T. Gressling, H.K. Muller-Buschbaum, Z. Naturforsch. 50 (1995) 1513–1516.
[4] M. Gärtner, D. Abeln, A. Pring, M. Wilde, A. Reller, J. Solid State Chem. 111 (1994) 128–133.
[5] D.H. Templeton, A. Zalkin, Acta Crystallogr. 16 (1963) 762–766.
[6] A.F. Van den Elzen, G.D. Rieck, Acta Crystallogr. 29 (1973) 2433–2436.
[7] J.M. Moreau, R.E. Gladyshevskii, Ph. Galez, J.P. Peigneux, M.V. Korzik, J. Alloys Compd. 284 (1999) 104–107.
[8] T. Easka, Solid State Ionics 52 (1992) 319–325.
[9] T. Easka, Solid State Ionics 136–137 (2000) 1–9.
[10] S. Takai, S. Touda, K. Oikawa, K. Mori, S. Torii, T. Kamiyama, T. Esaka, Solid State Ionics 148 (2002) 123–133.
[11] F. Dubois, F. Goutenoire, Y. Lalligant, E. Suard, P. Lacorre, J. Solid State Chem. 159 (2001) 228–233.
[12] F. Goutenoire, O. Isnard, E. Suard, O. Bohnke, Y. Laligant, R. Retoux, P. Lacorre, J. Mater. Chem. 11 (2001) 119–124.
[13] F. Goutenoire, O. Isnard, R. Retoux, P. Lacorre, Chem. Mater. 12 (2000) 2575–2580.
[14] P. Lacorre, F. Goutenoire, O. Bohnke, R. Retoux, Y. Lalligant, Nature 404 (2000) 856–858.
[15] J.P. Fournier, R. Kohlmuller, Bull. Soc. Chim. Fr. 12 (1970) 4277–4279.
[16] J. Rodriguez-Carvajal, in: Collected Abstracts of Powder Diffraction Meeting, Toulouse, France, 1990, p. 127.
[17] J. Gonzalez-Platas, J. Rodriguez-Carvajal, Graphic Fourier Program Vol. 1.12, Laboratoire Léon Brillouin, CEA-CNRS, Centre d'Etudes de Saclay, France.
[18] P. Stadelmann, Ultramicroscopy 14 (1981) 149.
[19] I.D. Brown, D. Altermatt, Acta Crystallogr. B 41 (1985) 244.
[20] N.E. Brese, M. O'Keeffe, Acta Crystallogr. B 47 (1991) 192.
[21] A.F. Wells, Structural Inorganic Chemistry, 3rd Edition, Clarendon Press, Oxford, 1962, p. 446 (Chapter 10).
[22] C. Desportes, et al. Electrochimie des Solides, Presses Universitaires de Grenoble, 1994.